

## **Erosion-corrosion degradation of additively manufactured metals**

Joshua Owen, Jasper Alderton, Joshua Greaves, Tsun Yu Brian Li, Josh Maddison,  
Robert Patton, Richard Barker, Robert Kay  
School of Mechanical Engineering, University of Leeds  
Leeds, LS2 9JT, United Kingdom

Yogiraj Pardhi  
Sulzer Pumps UK Ltd  
Manor Mill Lane  
Beeston, Leeds  
LS11 8BR  
United Kingdom

### **ABSTRACT**

Metals and alloys produced by additive manufacturing (AM) are becoming more widely utilized across a number of industrial applications such as energy generation, flow machinery and aerospace. Questions remain, however, with regards to their degradation resistance when compared to conventionally manufactured equivalents. One form of material degradation that has yet to receive wider attention is erosion-corrosion of AM metals, a degradation mechanism that occurs in particle-laden corrosive fluids. The erosion-corrosion degradation of AM metals and their conventionally manufactured counterparts has been investigated in this study by using both experimental and computational methodologies. The degradation of AM nickel alloy 625 (UNS N06625) was compared with a conventionally manufactured equivalent within a submerged impingement jet (SIJ) at flow velocities of 10 m/s and 20 m/s, in ambient aqueous conditions containing sodium chloride and sand particles. To characterize the behavior of the fluid and the sand particles in the SIJ, a computational fluid dynamics model was developed to predict particle impingement angles and velocities at the test coupon surface. In combination with experimental results and surface analysis of the resulting wear scar, wear maps were constructed to compare the operational window for AM and conventionally manufactured equivalents in erosion-corrosion conditions. AM nickel alloy 625 generally experienced greater erosion-corrosion degradation rates at lower impingement angles compared to the conventionally manufactured equivalent but was also found to work-harden to a greater extent at high impingement angles.

**Key words:** additive manufacturing, erosion, erosion-corrosion, computational fluid dynamics, surface interferometry

## INTRODUCTION

Degradation of materials in fluid transport systems is a critical issue faced by many industries where mass laden and corrosive fluid flow transport are required.<sup>1-6</sup> In such environments, severe degradation rates can be observed.<sup>4</sup> Recently there has been considerable investment into the applications of metals and alloys produced by additive manufacturing (AM) as this enables the fabrication of complex geometries from materials that would conventionally be difficult to manufacture. However, questions remain with regards to the degradation resistance of metal components produced by AM, with research dedicated to proving equivalence to metals produced by traditional manufacturing techniques.<sup>7</sup>

One area of interest for AM metals is their application in environments where erosion-corrosion degradation could occur, a degradation mechanism which has yet to receive significant attention in the assessment of AM metals. Erosion-corrosion is a wear mechanism that occurs due to the presence of erosion and corrosive substances within the transport fluid. Erosion occurs due to solid particulates, such as sand, impacting on a surface and removing the impacted material from the bulk surface.<sup>8,9</sup> This can be especially detrimental at changes in flow geometry or regions of accelerated flow (for example, in flow machinery), where the impingements from particulates could become focused in one region.<sup>10</sup>

Many studies have been conducted to establish the link between erosion and corrosion when combined in an overall erosion-corrosion wear mechanism, investigating the synergy between erosion and corrosion that occurs, as described in Equation (1).<sup>4,11</sup> It has been observed on numerous occasions that erosion can enhance corrosion rates ( $\Delta C_E$ ) and that corrosion can enhance erosion ( $\Delta E_C$ ).<sup>12</sup>

$$EC = E + C + \Delta E_C + \Delta C_E \quad (1)$$

where EC is the overall erosion-corrosion degradation rate and E and C represent the pure erosion and corrosion, respectively.

A number of mechanisms have been proposed that explain the synergistic effects between erosion and corrosion, including the breakdown of the passive layer as a result of particle impingement leading to enhanced corrosion, whilst corrosion of work hardened layers makes the material more susceptible to erosion.<sup>8</sup>

With regards to mitigating erosion-corrosion, traditional approaches such as surface coatings<sup>6</sup> and corrosion inhibitors<sup>13</sup> have been employed to reduce degradation rates. However, the success of these approaches can be limited in some demanding environments, notably by the geometric complexity of the component exposed to erosion-corrosion.<sup>14</sup> AM also enables the creation of materials with refined mechanical characteristics, such as hardness<sup>15</sup>, which has a significant influence on the erosion resistance of a material.<sup>16</sup> This, therefore, enables the possibility of creating AM materials with improved resistance to erosion-corrosion degradation. However, the characteristics and behaviors of AM materials are not fully known and the resistance to corrosion, erosion and erosion-corrosion are largely dependent on the fabrication method and heat treatments post-fabrication.<sup>17</sup>

A recent study by Laleh et al.<sup>18</sup> found that AM 316L stainless steel exhibited reduced combined erosion-corrosion resistance compared to conventionally manufactured equivalents. The cause of this was explained by the conventional material demonstrating faster repassivation kinetics, despite having a reduced resistance to pitting corrosion and lower hardness than the AM material. Aside from this study, there has been limited investigations of erosion-corrosion of AM materials reported in literature. Therefore, further research is needed to understand these behavior of AM materials, and in particular, their resistance to erosion-corrosion degradation.

In this study, a combined experimental and computational approach was performed to evaluate the erosion-corrosion resistance of AM materials through comparison with a conventionally manufactured equivalent material. By building a model of a corresponding submerged impinging jet (SIJ) apparatus

used for experiments, computational fluid dynamics (CFD) provided insights into the complex flow regime and underlying erosion-corrosion mechanisms. Combination of the experimental and analytical results then allowed wear maps to be constructed for erosion-corrosion degradation of these metals.

## EXPERIMENTAL PROCEDURE

### Material Preparation

Nickel alloy 625 (UNS N06625) was used for the material comparison in this study. Alloy 625 is commonly employed in environments requiring excellent resistance to erosion and corrosion.<sup>19</sup> A comparison was made between a conventionally manufactured alloy and AM equivalent produced by Laser-Powder Bed Fusion (L-PBF). No heat treatment was applied to the materials. Scanning electron microscope (SEM) images of the two materials are compared in Figure 1 after cross-sectioning using a focused ion beam. Similar microstructural features (in terms of approximate grain size) can be observed in the cross-sections between the AM material and conventional material. This similarity has previously been reported for nickel alloy 625.<sup>20, 21</sup> Energy dispersive X-ray spectroscopy identified a region rich in titanium on the conventional material cross-section, likely a titanium nitride inclusion.<sup>22</sup> Coupons were machined to expose a surface area of 5.56 cm<sup>2</sup> and 2.29 cm<sup>2</sup> for the conventional and AM metals respectively. Coupons were prepared for experiments by wet-grinding using silicon carbide grinding paper progressively (up to P800) before rinsing with acetone and deionized water prior to drying with compressed air and mounting in experimental apparatus. Prior to testing, the mass of each coupon was determined using a mass balance with a resolution  $\pm 0.1$  mg, after grinding. After testing, samples were rinsed and dried, and mass loss measurements were taken to determine the rate of degradation during the experiment.

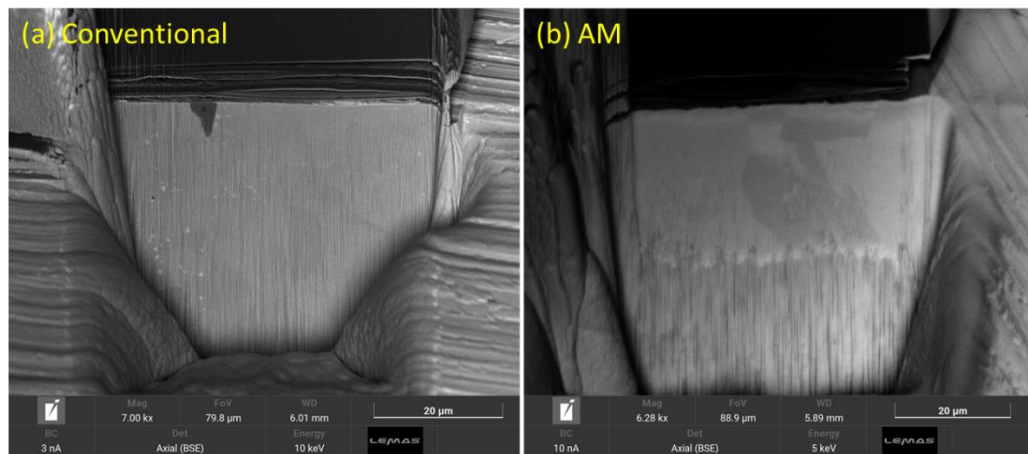


**Figure 1: Comparison of (a) the conventionally manufactured and (b) AM nickel alloy 625 microstructure using an SEM**

### Submerged Impinging Jet Experiments

A SIJ was used for its capabilities to replicate corrosion, erosion and erosion-corrosion conditions with varying fluid velocities and sand concentrations. The rig includes a 50 L capacity tank attached to a pump which distributes the fluid through the system, as shown in Figure 2. The fluid exits via two 4 mm diameter nozzles and contacts the metal coupons at a distance of 5 mm, held in place by two sample holders. For pure erosion tests, nitrogen was bubbled through the solution for 12 hours prior to, and throughout, the experiment to remove dissolved oxygen from the water. All experiments were performed for a period of 3 h.

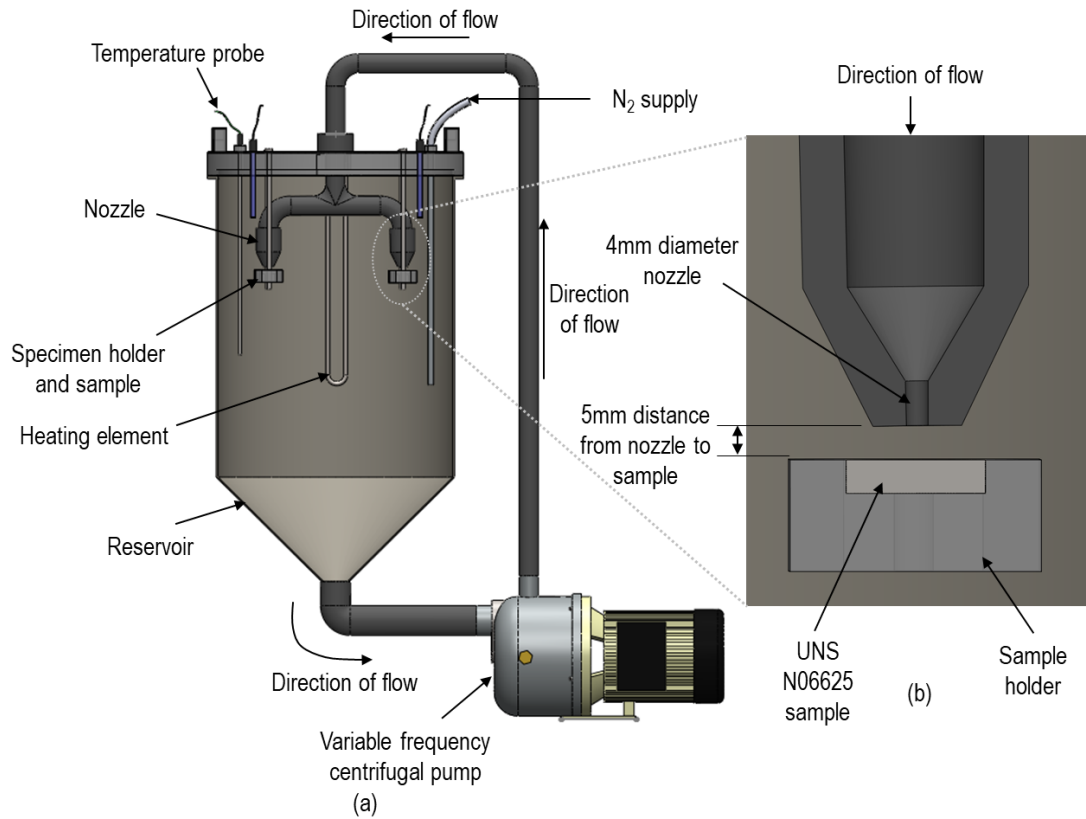


**Figure 2: SIJ used for erosion, corrosion and erosion-corrosion experiments, showing (a) the full SIJ apparatus and (b) a cross-section of the nozzle**

The temperature of the solution was maintained at 25°C and two fluid velocities were evaluated, 10 and 20 m/s. The fluid velocity was measured at the nozzle exit and calibrated with pump frequency prior to experimenting. Three types of tests were completed, pure erosion, pure corrosion, and erosion-corrosion. To replicate sea water pumping environments subject to particle impingement, 3.5 wt.% of sodium chloride (NaCl) was added to the reservoir, which was filled with 50 L of aerated water. Under pure erosion experimental conditions, NaCl was not added to the solution. Sand particles were used as the erodent for erosion and erosion-corrosion experiments and added to the 50 L solution. The sand particles were rounded in shape and the average particle diameters was ~800  $\mu\text{m}$ , as shown in the scanning electron microscope (SEM) and particle size measurements in Figure 3.<sup>23</sup>

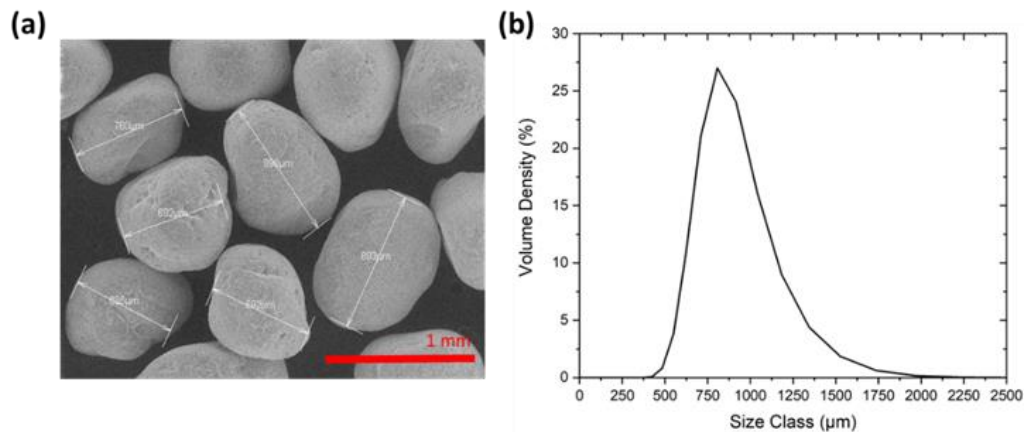


**Figure 3: (a) SEM image and (b) size distribution of sand particles used.**

## Surface Analysis

Test coupons were characterized prior to testing, following preparation, with the average Vickers Hardness measured at various points on the surface using a Mitutoyo HM-122<sup>†</sup> micro-indenter. Wear scars were analyzed using a Bruker NPFLEX<sup>†</sup> white light interferometer, with precision of 0.02  $\mu\text{m}$ , to extract topographical data.

## COMPUTATIONAL FLUID DYNAMICS PROCEDURE

A computational fluid dynamics (CFD) model of the SIJ apparatus was developed using COMSOL Multiphysics<sup>†,24</sup> to provide analytical flow and erosion data to supplement the experimental analysis. First the geometry and boundary conditions of the jet were defined, followed by details of the particle tracing model setup.

### Geometry and Boundary Conditions

The SIJ geometry was modelled with a 2D axis of rotational symmetry, as demonstrated in Figure 4, enabling efficient use of computational resources whilst still obtaining accurate results. The test coupon and sample holder were modelled with a 25 mm radius. The sample surface was assumed to be flat. A standard k- $\omega$  turbulence model was selected based on recommendations in previous studies for SIJ models, with a turbulence intensity of 0.05 and a turbulence length scale of  $3 \times 10^{-4}$ .<sup>4</sup>

The fluid domain was set as water, with a density of  $997 \text{ kg/m}^3$  and a dynamic viscosity of  $0.89 \text{ mPa}\cdot\text{s}$  to replicate the experimental conditions. The inlet flow velocity was set to either 10 or 20 m/s, with an outlet static gauge pressure of 0 Pa. The walls of the geometry were assumed to have no slip, with no roughness modelling included.

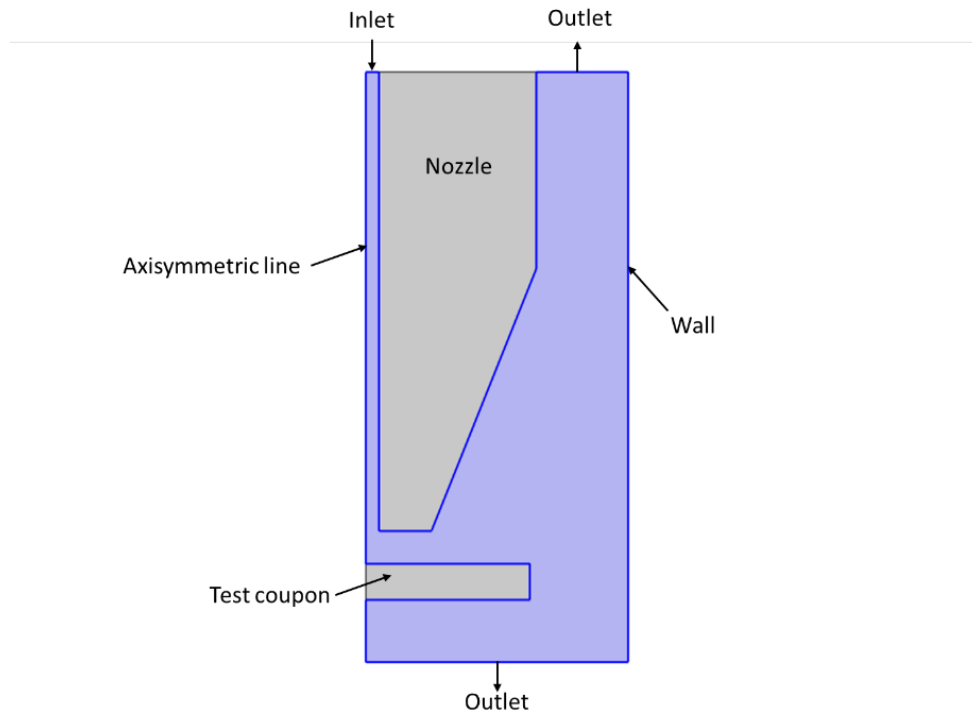


**Figure 4: 2D axisymmetric model of the SIJ used in the CFD model.**

<sup>†</sup> Trade name

A structured mesh containing 81,911 elements was selected for this SIJ model as it aided solution convergence, offering increased accuracy and a reduced solver time. Triangular elements were used as they allow for finer mesh adjustments and ensure elements have alignment with the flow direction. A boundary layer composed of rectangular elements was generated around the walls, with focused refinement in areas with high velocity gradients, such as the wall of the nozzle and along the surface of the sample. Element biases were used to refine the mesh in those regions. A mesh sensitivity analysis was completed to confirm independence of the solution from the mesh resolution. Particles used in the model were assumed to be spherical and have a diameter of 800  $\mu\text{m}$ .

## **Wear Maps**

Wear mapping of erosion data, as reported by Gnanavelu et al.<sup>25</sup>, can be used to predict wear in complex geometries. However, application of these wear maps has been limited to conventional materials and generally erosion-only conditions. Wear maps can aid the understanding of AM materials in erosion-corrosion environments, in addition to better predicting degradation rates in complex geometries. Wear maps were produced by combining the analytical particle impact and velocity data from the CFD model with wear scar data from the experimental testing for the 10 m/s and 20 m/s flow velocities. The 3D scattered data was then collected, and bilinear interpolation performed over a regular grid of particle impingement velocities and angles to produce wear maps.

## **RESULTS**

### **Experimental Results**

Mass loss measurements obtained from SIJ experiments under erosion, corrosion and erosion-corrosion conditions are shown in Figure 5. Mass loss measurements were averaged, with the maximum and minimum values reported as error bars. Large increases in mass loss are observed as flow velocity is increased from 10 to 20 m/s, with minimal corrosion degradation measured in corrosion-only experiments. Corrosion rates were generally negligible, however, marginally increased corrosion resistance is exhibited by the AM metal at both velocities. Erosion resistance was found to be slightly greater for the conventional material. The influence of sand concentration in these conditions is characterized by a large increase in mass loss, with erosion increasing by a factor of  $\sim 2$  for conventional and AM materials at a sand concentration of 1000 mg/L compared to a concentration of 500 mg/L. For overall erosion-corrosion degradation, the mass loss approximately doubled when the sand concentration was increased from 500 mg/L to 1000 mg/L. At a flow velocity of 10 m/s and sand concentration of 500 mg/L, an increase in mass loss, potentially due to the synergistic effects between erosion and corrosion, was observed for AM and conventional materials. However, at 10 m/s and 1000 mg/L of sand, and at 20 m/s, no significant enhancement is seen.

Work hardening was evaluated by performing indentation testing on the test coupons after the erosion and erosion-corrosion experiments. The average hardness from multiple measurements inside the center of the wear scar (showed later in profilometry measurements) was obtained and compared with the hardness in the outer regions of the coupon, where no erosion damage was observed. The percentage increases in hardness (i.e. the hardness inside the wear scar, compared to outside) are shown in Figure 6. The AM materials experienced increased work hardening in all conditions, which resulted in a larger final wear scar hardness. Generally, lower hardness was observed in erosion-corrosion conditions than in erosion conditions. There was very no significant enhancement seen at either sand concentration.

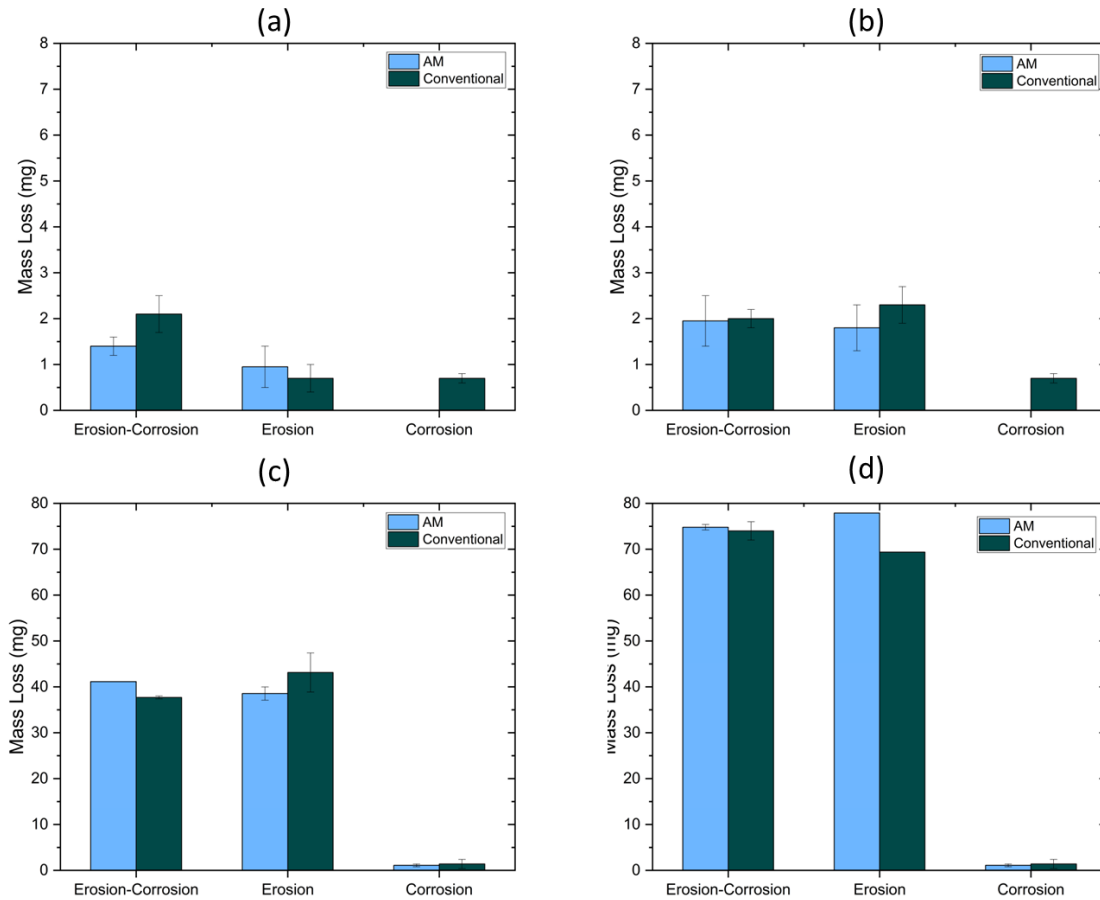


**Figure 5: Mass loss measurements after 3 h erosion, corrosion and erosion-corrosion experiments were performed in an SIJ containing water at 25°C under sand concentration and flow velocity conditions of: (a) 500 mg/L, 10 m/s and (b) 1000 mg/L, 10 m/s, (c) 500 mg/L, 20 m/s and (d) 1000 mg/L, 20 m/s. Note: y-axis scale is 10x smaller for 10 m/s experiments**

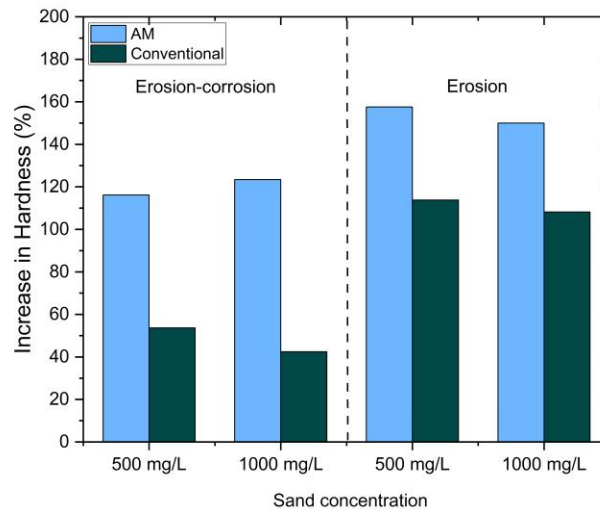


**Figure 6: Hardness measurements after 3 h erosion and erosion-corrosion experiments were performed in an SIJ containing water at 25 °C, recirculating at flow velocities of 20 m/s. Sand was added at concentrations of 500 mg/L and 1000 mg/L.**

## Wear Scar Analysis

Wear scar profiles were obtained for erosion and erosion-corrosion conditions, shown in Figure 7, at a flow velocity of 20 m/s. A typical W-shaped wear scar is observed. The AM material was found to be marginally less erosion resistant than the conventional material, confirmed by the wear scars in Figure 7. The influence of sand concentration is prominent on the wear scar depth, almost doubling the maximum depth for all test conditions when the sand concentration is increased from 500 mg/L to 1000 mg/L. At 20 m/s wear depth was ~10% deeper in erosion and erosion-corrosion conditions for the AM material.

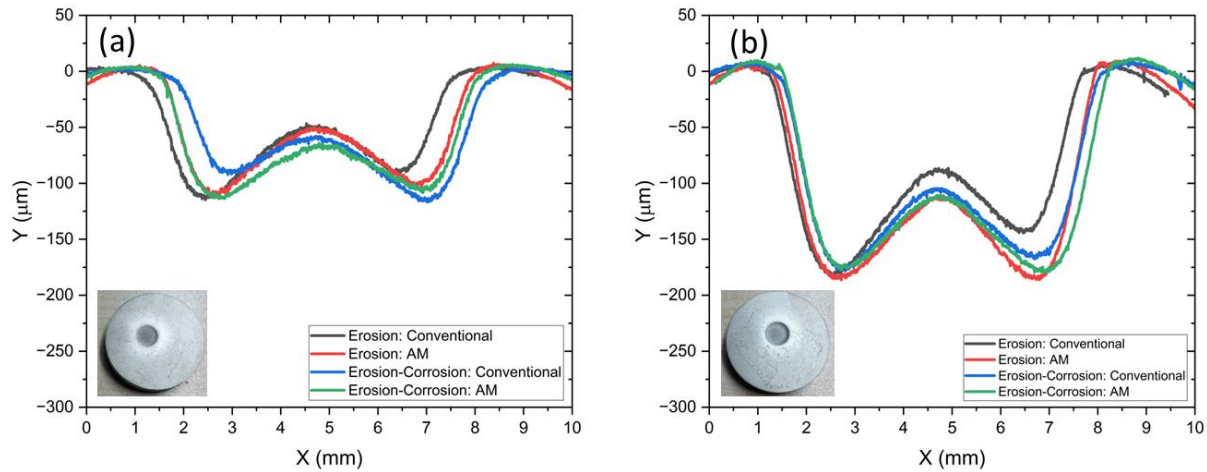


**Figure 7: Wear profiles after 3 h erosion and erosion-corrosion experiments were performed in an SIJ containing water at 25 °C, recirculating at a flow velocity of 20 m/s and containing a sand particle concentration of (a) 500 mg/L and (b) 1000 mg/L. Images of the conventional material after erosion-corrosion experiments are included on the plots.**

## CFD Model Results

The CFD model was then utilized to characterize the specific particle impingement angles and impingement velocities across the test material surface, resulting in the wear depths observed in Figure 7. An example of the fluid flow through the SIJ nozzle is shown in Figure 8 for a flow velocity of 20 m/s, where the focus is on the flow exiting the nozzle and impinging onto a surface. This replicates the test material surface, as demonstrated in Figure 2 and Figure 4. As the flow exits the nozzle, a high flow velocity region is initially observed before the flow spreads across the target surface. In the center of the sample surface, a stagnation region is observed,<sup>4, 25</sup> where the flow velocity decreases significantly as the flow path changes. As the radial distance increases from the center of the nozzle, the flow velocity once again increases, and a highly turbulent region is observed at approximately 2-4 mm from the center. Beyond this point, the flow continues to spread and the flow velocity reduces.

Once the fluid flow model was complete, particle modelling could be performed by coupling the particle motion equations to the fluid flow velocity field. This enabled particles to be tracked as they move through the flow field and towards the test coupon surface. Subsequently, particle impingement data can be generated at the sample surface. The particle impingement velocity and particle impingement angle at a flow velocity of 20 m/s are shown in Figure 9. At the center of the nozzle, in the stagnation region, a high number of particle impingements occur. In this region, particle impingement angles are also high, meaning that particles generally impinge onto the surface at angle of  $>80^\circ$  but at a relatively low velocity (~12-13 m/s). Further from the center of the sample, the particle impingement velocity increases, to a maximum at approximately 2.5 mm from the center. This correlates with the higher turbulence region observed in Figure 8. At the higher velocities, the impingement angle has also decreased.



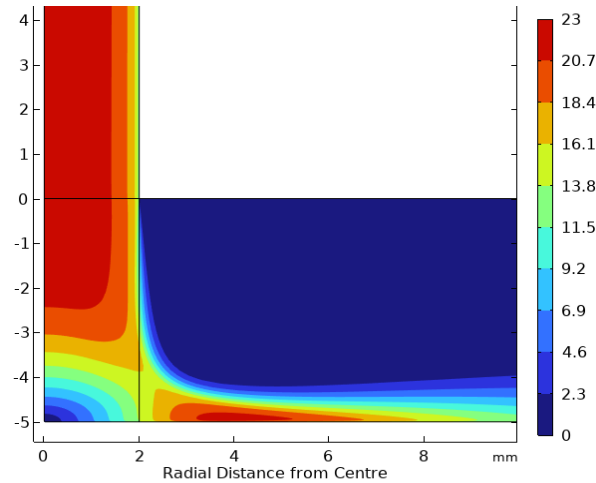


**Figure 8: CFD model of flow velocity (m/s) in an SIJ with a mean inlet flow velocity of 20 m/s.**

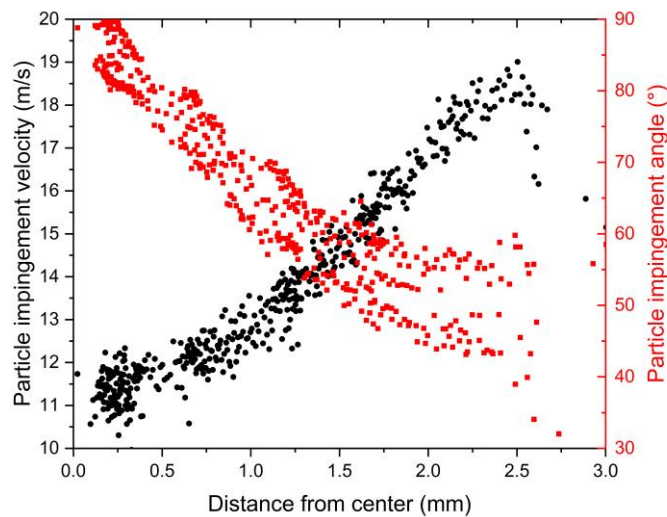


**Figure 9: CFD model of impact angle and impact velocity on a sample in an SIJ with a mean inlet flow velocity of 20 m/s.**

When comparing the CFD model results in Figure 8 and Figure 9, several features can be observed that relate the flow characteristics of the SIJ to the resulting wear scars that were measured in Figure 7. Whilst there is a high probability of particle impingement in the center of the nozzle, particle impingement events will mostly be high impingement angle and therefore lead to work hardening, as opposed to material degradation.<sup>26, 27</sup> These particle impingement events are also generally at a lower velocity than other impingements, therefore degradation is generally lower in this region. This was observed in the wear scars in Figure 9, with the typical W-shaped profile observed and lower degradation in the center of the coupons. Higher velocity, lower angle impingements were observed further from the center. Under those conditions, it is expected that a greater amount of ‘cutting’ will be observed, whereby the particles cut into the material surface and cause much higher rates of degradation, compared to high angle impacts.<sup>26, 28</sup> This is also observed in the wear profiles in Figure 7, where the wear depth increases in the higher turbulence region.

### Wear Map Results

One of the most useful outputs of the CFD model is that the impingement angle and impingement velocity data can be utilized to construct wear maps. The wear maps were constructed for the conventional and

AM materials at a flow velocity of 20 m/s and sand concentration of 500 mg/L and 1000 mg/L, utilizing the CFD data reported in Figure 9 and the wear profile data in Figure 7. The wear maps are shown in Figure 10 for erosion and erosion-corrosion conditions, with blue regions representing the lowest rates of degradation. When comparing the AM material against the conventional material, the degradation behavior is generally similar. However, it does appear that the AM material is more susceptible to cutting erosion, whilst the higher rates of work hardening, as demonstrated in Figure 6, indicate greater resistance to high impingement angle erosion.

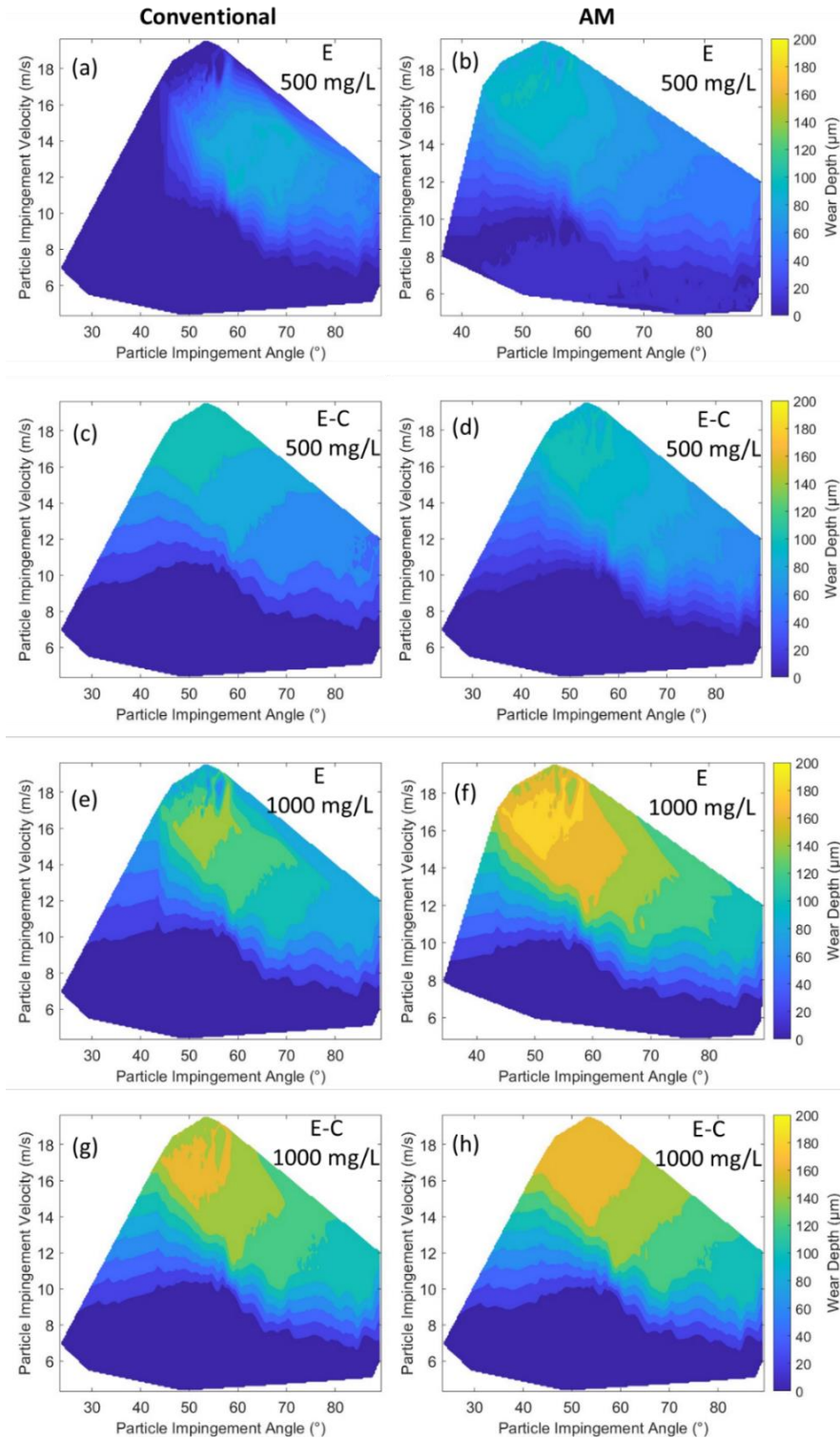


**Figure 10: Wear maps for (a,c,e,g) conventional and (b,d,f,h) AM materials using wear depth experimental data after erosion (labelled E) and erosion-corrosion (labelled E-C) experiments**

## CONCLUSIONS

This study presents a comprehensive analysis into the erosion-corrosion degradation of nickel alloy 625 (UNS N06625), produced by conventional manufacturing and AM techniques. Through a series of experimental and computational investigations, the main findings from the study were:

- Similar erosion-corrosion degradation rates were observed between the AM and conventionally manufactured nickel alloy.
- The AM alloy is slightly less erosion resistant than a conventionally manufactured equivalent, likely attributed to a lower initial hardness for the AM material.
- The hardness of the conventionally manufactured material was initially greater than the AM material, though the AM material experienced work hardening at a significantly enhanced rate in the center of the wear scar (high particle impingement angles), resulting in a harder wear scar than the conventional material.
- A CFD model was utilized to predict impingement velocities and angles of the particles in the SIJ flow. This enabled the construction of wear maps for the erosion and erosion-corrosion resistance of AM vs conventionally manufactured materials.
- When evaluating the wear maps, it demonstrated that the significant work hardening resulted in greater resistance to erosion degradation at high impingement angles for the AM material but appeared to show greater susceptibility to lower impingement angle cutting erosion.

## ACKNOWLEDGEMENTS

The authors would like to thank Stuart Micklethwaite at University of Leeds Electron Microscopy and Spectroscopy Centre (LEMAS) for SEM imaging.

## REFERENCES

1. S. Kairy, S. Zhou, A. Turnbull and G. Hinds. Corrosion of pipeline steel in dense phase CO<sub>2</sub> containing impurities: A critical review of test methodologies. *Corrosion Science*. 2023, **214**, p.110986.
2. S. Karlsdottir, K. Ragnarsdottir, A. Moller, I. Thorbjornsson and A. Einarsson. On-site erosion–corrosion testing in superheated geothermal steam. *Geothermics*. 2014, **51**, pp.170-181.
3. J. Owen, E. Ducker, M. Huggan, C. Ramsey, A. Neville and R. Barker. Design of an elbow for integrated gravimetric, electrochemical and acoustic emission measurements in erosion-corrosion pipe flow environments. *Wear*. 2019, **428-429**, pp.76-84.
4. J. Owen, C. Ramsey, R. Barker and A. Neville. Erosion-corrosion interactions of X65 carbon steel in aqueous CO<sub>2</sub> environments. *Wear*. 2018, **414-415**, pp.376-389.
5. E.V. Senatore, W. Taleb, J. Owen, Y. Hua, J.A.C.P. Gomes, R. Barker and A. Neville. Evaluation of high shear inhibitor performance in CO<sub>2</sub>-containing flow-induced corrosion and erosion-corrosion environments in the presence and absence of iron carbonate films. *Wear*. 2018, **404-405**, pp.143-152.
6. L. Vivar Mora, A. Taylor, S. Paul, R. Dawson, C. Wang, W. Taleb, J. Owen, A. Neville and R. Barker. Impact of silica nanoparticles on the morphology and mechanical properties of sol-gel derived coatings. *Surface and Coatings Technology*. 2018, **342**, pp.48-56.

7. G. Sander, J. Tan, P. Balan, O. Gharbi, D. Feenstra, L. Singer, S. Thomas, R. Kelly, J.R. Scully and N. Birbilis. Corrosion of additively manufactured alloys: a review. *CORROSION*. 2018, **74**(12), pp.1318-1350.
8. R.J.K. Wood and S.P. Hutton. The synergistic effect of erosion and corrosion: trends in published results. *Wear*. 1990, **140**(2), pp.387-394.
9. B. McLaury, J. Wang, S. Shirazi, J. Shadley and E. Rybicki. Solid particle erosion in long radius elbows and straight pipes. In: *SPE Annual Technical Conference and Exhibition, San Antonio, TX*. Society of Petroleum Engineers, 1997.
10. B.S. McLaury, S.A. Shirazi and T.L. Burden. Effect of Entrance Shape on Erosion in the Throat of Chokes. *Journal of Energy Resources Technology*. 2000, **122**(4), pp.198-204.
11. S. Aribo, R. Barker, X. Hu and A. Neville. Erosion–corrosion behaviour of lean duplex stainless steels in 3.5% NaCl solution. *Wear*. 2013, **302**(1), pp.1602-1608.
12. R.J.K. Wood. Erosion–corrosion interactions and their effect on marine and offshore materials. *Wear*. 2006, **261**(9), pp.1012-1023.
13. R. Barker, X. Hu, A. Neville and S. Cushnaghan. Inhibition of flow-induced corrosion and erosion–corrosion for carbon steel pipe work from an offshore oil and gas facility. *CORROSION*. 2012, **69**(2), pp.193-203.
14. R.P. Chaudhary, C. Parameswaran, M. Idrees, A.S. Rasaki, C. Liu, Z. Chen and P. Colombo. Additive manufacturing of polymer-derived ceramics: Materials, technologies, properties and potential applications. *Progress in Materials Science*. 2022, **128**, p.100969.
15. J. Zuback and T. DebRoy. The hardness of additively manufactured alloys. *Materials*. 2018, **11**(11), p.2070.
16. Y.I. Oka, M. Matsumura and T. Kawabata. Relationship between surface hardness and erosion damage caused by solid particle impact. *Wear*. 1993, **162**, pp.688-695.
17. G. Sander, V. Cruz, N. Bhat and N. Birbilis. On the in-situ characterisation of metastable pitting using 316L stainless steel as a case study. *Corrosion Science*. 2020, **177**, p.109004.
18. M. Laleh, A.E. Hughes, W. Xu, I. Gibson and M.Y. Tan. Unexpected erosion-corrosion behaviour of 316L stainless steel produced by selective laser melting. *Corrosion Science*. 2019, **155**, pp.67-74.
19. A. Neville and T. Hodgkiess. Characterisation of high-grade alloy behaviour in severe erosion–corrosion conditions. *Wear*. 1999, **233-235**, pp.596-607.
20. J.A. Gonzalez, J. Mireles, S.W. Stafford, M.A. Perez, C.A. Terrazas and R.B. Wicker. Characterization of Inconel 625 fabricated using powder-bed-based additive manufacturing technologies. *Journal of Materials Processing Technology*. 2019, **264**, pp.200-210.
21. D. Li, Q. Guo, S. Guo, H. Peng and Z. Wu. The microstructure evolution and nucleation mechanisms of dynamic recrystallization in hot-deformed Inconel 625 superalloy. *Materials & Design*. 2011, **32**(2), pp.696-705.
22. K.-H. Lim, K. Ryou, J.-H. Choi, G. Choi, W.S. Choi, J.-H. Lee, C.-S. Oh, P.-P. Choi and G.-D. Sim. Effect of titanium nitride inclusions on the mechanical properties of direct laser deposited Inconel 718. *Extreme Mechanics Letters*. 2023, **61**, p.102009.
23. R. Bhamji, J. Owen, M. Huggan, S. Marcelin, B. Normand and R. Barker. Electrochemical Investigation on localised corrosion under silica sand deposit layers of carbon steel within a bespoke test cell. *Corrosion Science*. 2023, p.111744.
24. COMSOL. *COMSOL Multiphysics 6.0 CFD Module User's Guide*. 2023.
25. A. Gnanavelu, N. Kapur, A. Neville and J.F. Flores. An integrated methodology for predicting material wear rates due to erosion. *Wear*. 2009, **267**(11), pp.1935-1944.
26. J.G.A. Bitter. A study of erosion phenomena part I. *Wear*. 1963, **6**(1), pp.5-21.
27. J.G.A. Bitter. A study of erosion phenomena: Part II. *Wear*. 1963, **6**(3), pp.169-190.
28. I. Finnie. Some observations on the erosion of ductile metals. *Wear*. 1972, **19**(1), pp.81-90.